NMR ANALYSIS OF THE STRUCTURE, DYNAMICS, AND UNIQUE OLIGOMERIZATION PROPERTIES OF THE HUMAN CHEMOKINE CTACK/CCL27

A. Jansma[1,2]*, J.P. Kirkpatrick[3]*, A. Hsu[1], T.M. Handel[1+], D. Nietlispach[3+]

[1]Skaggs School of Pharmacy and Pharmaceutical Science, University of California, San Diego, 9500 Gilman Drive, La Jolla, California 92093-0684

[2]Department of Chemistry and Biochemistry, University of California, San Diego, 9500 Gilman Drive, La Jolla, California 92093-0684

[3]Department of Biochemistry, University of Cambridge, 80 Tennis Court Road, Cambridge CB2 1GA, UK

*These authors contributed equally

[+]Address correspondence to: T.M. Handel (thandel@ucsd.edu)
and D. Nietlispach (dn206@bioc.cam.ac.uk)

Supplemental Experimental Procedures

Protein Expression and Purification – MOPS minimal media at 10x (1 L) was prepared with 400 mL of 1 M MOPS, 40 mL of 1 M Tricine, pH 7.4, with 10 mL of each of the following: 0.01 M $FeSO_4$, 0.276 mM K_2SO4, 0.5 M $CaCl_2$, 0.528 M $MgCl_2$, 5 M NaCl and Micronutrients, which contained 2.48 mg H_3BO_3, 0.47 mg $CoSO_4$, 0.17 mg $CuCl_2$, 1.58 mg $MnCl_2$ and 0.28 mg $ZnSO_4$ (the 10x mixture was then autoclaved). Each liter of 1x MOPS was made by combining 100 mL 10x MOPS and 10 mL 0.132 M Potassium Phosphate buffer at pH 7.4, followed by autoclaving. For labeled samples, 2 g $(^{15}NH_4)_2SO_4$ and 2.5 g ^{13}C-glucose were steri-filtered prior to adding. To initiate purification, cells were lysed by sonication and lysozyme treatment, and the insoluble fraction was pelleted by centrifugation. The insoluble fraction was then washed once with buffered detergent before being solubilized with the guanidine hydrochloride, and passed over a gravity Ni-NTA column (Qiagen). Chemokine containing fractions were eluted with low pH, pooled, and refolded by dilution into Hampton Fold-it Buffer #13. The protein was then dialized into buffer and concentrated by passing again over a Ni-NTA (Qiagen) column using an FPLC system (GE Healthcare). Protein fractions were eluted with imidazole and dialyzed overnight into 50 mM Hepes, pH 7.2. The His-ubiquitin tag was cleaved by the specific protease, ubiquitinase, and passed over a 5 mL gravity Ni-NTA column (Qiagen). Flow through and 50 mM imidazole washes were collected containing the non-His-tagged protein. The final purification step involved reverse phase HPLC with a semi-prep C4 column. Chemokine fractions were lyophilized and stored at -80ºC until use. Purity was confirmed using MALDI mass spectrometry (MS) and label incorporation was verified by ESI MS.

PFG diffusion measurements – The gradient field strength was initially calibrated using a doped water sample (1). The DOSY macro employed a linear increase in gradient field strength from 2% - 95%, running 16 successive 1D proton experiments. Values for the diffusion time, d20 (Δ) and the gradient pulse length, p30 (δ*0.5) were 150 ms and 2.0 ms respectively. Water suppression was achieved using a combination of Watergate and pre-saturation sequences. The self-diffusion coefficients (D_s) were calculated using the Bruker program for DOSY experiments with manual integration for peaks at 7.0, 3.0, 2.0, and 0.7 ppm for each proton spectrum. The resulting decay curves were fit and the D_s values calculated using the equation:

$$I(g) = I(0) \exp [-(\gamma g \delta)^2 D(\Delta - (\delta/3))]$$

where I(0) is 4.167 x 10^{-1}, γ is 4.258 x 10^3 Hz/G, g was calibrated at 5.784 G/mm, δ was set to 4.0 ms, and Δ was set to 150 ms. The Stokes-Einstein equation estimates the theoretical ratio $D_{s,dimer}/D_{s,monomer}$ to be 0.75 (1).

Monomeric structure determination – The assignment experiments recorded were: ^{15}N HSQC, HNCA, intra-HNCA, HN(CO)CA, HNCACB, HN(CO)CACB, HNCO, HN(CA)CO and (H)NNH-NOESY, ^{13}C

HSQC, (H)CC(CO)NH-TOCSY and H(CC)(CO)NH-TOCSY (14.3 ms DIPSI mixing), TOCSY–^{15}N HSQC (43.3 ms DIPSI-2rc mixing), H(C)CH-TOCSY, methyl-selective H(C)CH-TOCSY and (H)CCH-TOCSY (18.6 ms FLOPSY-16 mixing). Partial side-chain assignment and connection between the backbone and side-chains was accomplished using 3D TOCSY–^{15}N HSQC, H(CC)(CO)NH and (H)CC(CO)NH experiments. Side-chain assignment was completed using the 3D H(C)CH-TOCSY experiment analyzed in conjunction with the constant-time ^{13}C-HSQC spectrum. The assignment of the HCCH-TOCSY spectrum in the crowded methyl regions was expedited by acquisition of methyl-selective implementations of both the H(C)CH- and (H)CCH-TOCSY 3D experiments, in which only methyl-type protons are detected during acquisition. Assignments for aromatic resonances were obtained from the ^{13}C-separated NOESY spectrum, aided by reference to a constant-time ^{13}C HSQC spectrum optimized for aromatic spin systems, as well as 2D NOESY spectra acquired with and without ^{15}N decoupling.

Identification and assignment of medium-range NOEs within helical secondary structure elements, and inter-strand NOEs within β-sheet regions were facilitated by the secondary structure prediction provided by the Chemical Shift Index (CSI) (2). Structure calculations were performed with ARIA (ambiguous restraints for iterative assignment) (3,4) interfaced to CNS (crystallography and NMR system) (5) Dihedral angle restraints were generated from the backbone chemical shifts using the program TALOS (6), and amide hydrogen bonds were included in the structure calculation as pseudo-NOE distance restraints. Amide hydrogen bond donors were determined using the CLEANEX experiment (7). In short helical regions and at the ends of long helices, both possibilities for the hydrogen bond acceptors were incorporated by modeling the hydrogen bonds as ambiguous distance restraints. The regiochemistry of the two disulfide bonds was determined by running a complete structure calculation in which no information on the disulfide bridges was initially provided, but once identified, they were used as distance restraints.

Nine iterations were performed for the final structure calculation. Of the 100 structures calculated in the last iteration, the 30 lowest in energy were selected for water refinement and analysis. For resolution of ambiguous distance restraints, the total contribution of the accepted NOEs to an ambiguous cross-peak was reduced during the calculation from 1.0 to 0.8. The number of ambiguous restraints was reduced from 1204 to 562 during the course of the structure calculation.

^{15}N relaxation measurements – Relaxation experiments for determination of the rotational diffusion tensor and characterization of the internal dynamics were recorded on 1.0 mM ^{15}N-labeled CCL27 at fields of 500 and 600 MHz. ^{15}N R_1 and R_2 relaxation rates, and [^{1}H]^{15}N heteronuclear NOEs were measured using standard pulse sequences. The transverse cross-correlation rate constant, η_{xy}, was measured using three methods: via cross-correlation-mediated interconversion of ^{15}N in-phase and anti-phase magnetization magnetization (at both 500 MHz and 600 MHz) (8), via selection of the two lines of the ^{15}N doublet (denoted H^{α} and H^{β}), and comparing their intensities (at 500 MHz only), and from the TROSY-selected spin echo experiment (at 600 MHz only).

Errors in the relaxation rate constants were estimated using a boot-strap method, which repeats the data-fitting many times with data-sets generated from the original data-sets by re-sampling with replacement. Errors in the heteronuclear NOE values were calculated from the peak intensities and noise levels in the reference and saturated spectra.

The rotational diffusion tensor was determined from the R_2^0/R_1 ratios for those residues that exhibited ^{1}H-^{15}N heteronuclear values greater than 0.60 at 500 MHz. R_2^0 rate constants were calculated from η_{xy} according to $R_2^0 = \kappa\eta_{xy}$, using values for κ of 1.423 and 1.292 at 500 MHz and 600 MHz, respectively. For the analysis at 500 MHz, η_{xy} rate constants were calculated as the averages of the two values obtained using the in-phase/anti-phase interconversion and H^{α}/H^{β} selection methods, with the uncertainties taken as the corresponding standard deviations. Similarly, η_{xy} rate constants at 600 MHz were calculated as the averages of the values obtained from the in-phase/anti-phase interconversion experiment and those extracted from the TROSY-selected spin-echo exchange experiment. The uncertainties in the R_1 rate constants used in the TENSOR2 analysis were taken to be twice those computed using the boot-strap procedure in CcpNmr analysis. Ignoring negligible contributions from

high-frequency spectral density terms, the measured η_{xy} values were converted to exchange-free R_2^0 rate constants using $k = R_2^0 / \eta_{xy} = (c^2 + d^2) / (cd(3\cos^2\theta - 1)$. The angles between the ^{15}N CSA tensor and the N–H bond, θ, was set at –17°, and the amide bond length, r_{NH}, was set at 1.02 Å. The errors in the magnitudes of the principal components of the diffusion tensor were computed from 500 simulated data-sets constructed through Monte-Carlo sampling of the Gaussian error distributions defined by the experimental uncertainties. These 500 data-sets were also used to generate the simulated χ^2 distribution, the value of which at the 95 % confidence interval was compared to the experimental χ^2 value to assess the agreement of the diffusion tensor model with the experimental data. The fitting of the internal mobility was performed for all residues with R_1, R_2^0 and NOE data using the fully anisotropic diffusion tensor.

Dimer and hydrodynamic modeling – The diffusion tensor for the CC-dimer model is significantly elongated, and would be closely approximated by a heavy prolate axially symmetric tensor. In contrast, the diffusion tensor for the CXC dimer is almost isotropic with a slightly prolate tensor the closest axially symmetric approximation. The primary hydrodynamic models were generated using an atomic element radius of 3.2 Å. Secondary shell modeling was performed for 6 values of the bead radius σ from 1.2 Å to 2.2 Å.

Exchange Broadening Calculations – $R_2(1/\tau_{ep})$ values were calculated from the intensities of the sub-spectra, $I(1/\tau_{cp})$, and that of the reference spectrum, I_{ref}:

$$R_2\left(1/\tau_{cp}\right) = \frac{1}{\Delta}\ln\left(\frac{I_{ref}}{I\left(1/\tau_{cp}\right)}\right)$$

where Δ is the length of the constant-time period (80 ms).

Exchange contributions at 600 MHz were also measured using a version of the TROSY-selected spin echo experiment described by *Wang, et. al.* (9). Three TROSY-type ^{15}N–^1H spectra are recorded such that the peak intensities are proportional to the relaxation rates $R(N_xH^\beta)$, $R(N_x/2N_yH_z)$ and $R(2N_zH_z)$. By rearranging the expression for the relaxation rate of the TROSY-line, R_{ex} can be written as:

$$R_{ex} = R(N_xH^\beta) + \eta_{xy} - \tfrac{1}{2}R(H_z) - R_2^0$$

For proteins with tm>4ns, $R_2^0 = \kappa\eta_{xy}$ and $R(H_z) = R(2N_zH_z) - R(N_z)$ and therefore:

$$R_{ex} = R(N_xH^\beta) - \eta_{xy}(\kappa - 1) - \tfrac{1}{2}R(2N_zH_z) + \tfrac{1}{2}R(N_z)$$

Since $\eta_{xy} = R(N_x/2N_yH_z) - R(M_xH^\beta)$, values for η_{xy} can be calculated from the peak intensities in the corresponding sub-spectra via:

$$\eta_{xy} = \frac{1}{2\tau}\ln\left(\frac{I(N_xH^\beta)}{I(N_x/2N_yH_z)}\right)$$

and therefore R_{ex} is given by:

$$R_{ex} = \frac{1}{2\tau}\ln\left(\frac{I(2N_zH_z)}{I(N_xH^\beta)}\right) - \frac{\kappa - 1}{2\tau}\ln\left(\frac{I(N_xH^\beta)}{I(N_x/2N_yH_z)}\right) + \frac{R(N_z)}{2}$$

The length of the relaxation delay is 2τ in the $R(N_xH^\beta)$ and $R(N_x/2N_yH_z)$ sub-spectra, and τ in the $R(2N_zH_z)$ sub-spectrum. $R(N_z)$ values are measured in a separate experiment.

Heparin Binding Assay – ^{125}I-CCL27 and unlabeled WT CCL27 at different concentrations were added to wells of a 96-well plate. 100 µg of Heparin-sepharose or Sepharose 6 Fast Flow was added to labeled and unlabeled chemokine in a final volume of 60 µL. The 96-well plate was covered and incubated for 2 hours at room temperature with gentle agitation. During this time, a GF/C filter plate was soaked in 0.5% polyethylinimine. After incubation, the filter plate was washed with 50 mM Hepes, pH 7.2, 5 mM $MgCl_2$, 1 mM $CaCl_2$, and 0.1% BSA. The contents of the 96-well plate were harvested onto the filter plate by aspiration, as were the contents of two subsequent washes of the 96-well plate with 200 µL of wash buffer. The filter plate was then immediately washed with 400 µL of wash buffer and allowed to dry under a heat lamp. After drying, 50 µL of scintillation fluid was added to each of the wells, the top and bottom of the filter plate were sealed, and the radioactivity counted with a scintillation plate reader.

Supplemental Results

Exchange broadening – While the TROSY-selected spin-echo experiment simply yields the R_{ex} contribution, the CPMG relaxation-dispersion data can be fitted to provide other exchange parameters, such as exchange rate, chemical shift differences and relative populations of the exchanging sites. Typically, this is obtained through the use of simplified fitting equations for $R_2(\nu_{CPMG})$ once the field dependence of the exchange regime has been determined (10). Approximation of the field dependence of R_{ex} by the effective transverse rates measured at the fasted and slowest CPMG pulsing rates ($R_2(\nu_{CPMG})$ = 7.7 Hz and $R_2(\nu_{CPMG})$ = 1000 Hz) at 500 and 600 MHz yielded a value $\alpha = 1.55$ for the proportionality between the fractional change in the exchange broadening and the small change in the applied field. This confirmed that with the exclusion of the C-terminal peaks in the ^{1}H-^{15}N HSQC spectrum the exchange process occurs on the intermediate-to-fast timescale. The relaxation-dispersion data was thus fitted according to an expression formulated by Luz and Meiboom, valid for exchange on the fast timescale (11) (see Materials and methods). Good agreement was found between the R_{ex} values extracted from standard and TROSY-type CPMG dispersion profiles and the TROSY-selected spin-echo exchange data acquired. For the dispersion profiles acquired using the standard CPMG sequence there was reasonable agreement between the data at the two fields with average k_{ex} of 1.11×10^3 s^{-1} ($\pm 0.52 \times 10^3$ s^{-1}) and 0.99×10^3 s^{-1} ($\pm 0.42 \times 10^3$ s^{-1}) at 500 and 600 MHz, respectively.

Comparison of the Experimental Rotational Diffusion Tensor with Theoretical CXC and CC Dimer Models – The properties of the rotational diffusion tensor calculated from exchange-free ^{15}N relaxation rates are determined by the size and shape of the molecule, and can thus provide information on both the stoichiometry and binding mode of an oligomeric state, provided the oligomeric complexes are significantly different enough in size and shape. As the isotropic rotational correlation time of 9.2 ns for the 1 mM sample translates into an average molecular weight approximately twice that of the CCL27 monomer, it suggested that this chemokine is predominantly dimeric at these concentrations. However, the simulated tensor properties of putative CC and CXC type dimer models which were constructed using an in-house docking program based on the monomer structure did not show sufficient agreement with the experimental data, even though the simulated tensors showed clear differences between the CC and CXC models (Supplemental Table 2 and 3). These results seem to be consistent with the assumption that CCL27 does not appear as a discrete dimer but rather exists in exchange between different oligomeric forms. The more concentrated 2.1 mM sample exhibited a longer correlation time of 13 ns, indicative of a larger ~ 30 kDa protein. The increase in the average molecular weight is most probably the result of dimer to tetramer oligomerization, with increased concentration shifting the equilibrium position toward the tetrameric species. While the observed rotational diffusion tensor at 1 mM corresponds more closely to that predicted for a CXC-type dimer it does not agree sufficiently with the experimental data to exclusively support such type of interaction. Assuming that a tetramer formation proceeds via a dimer stage, it could be postulated that at 1 mM the average species corresponds to dimeric CCL27 where after taking into account of the exchange data analysis both CC and CXC interfaces seem to be involved.

Under this model and at the NMR concentrations employed, the sample would be comprised predominantly of CCL27 dimers. Alternatively, the tetrameric species may be formed directly from the monomer, without proceeding via an intermediate dimeric state. If this were the case, then the measured average rotational correlation time is indicative of significant concentrations of monomer and tetramer, and hence all the measured relaxation rates would be weighted averages of the rates characterizing the monomeric and tetrameric species. In such a situation the relative concentrations of monomer and tetramer required to reproduce the observed rotational correlation time can be estimated by writing the total rotational correlation function as a linear combination of the individual correlation functions for the monomer and tetramer, and equating to an apparent single-species correlation function:

$$C(\tau) \sim x \exp(-\tau/\tau_m) + (1 - x) \exp(--\tau/k\tau_m) = \exp(-\tau/\tau_m^{obs})$$

where x is the fractional proportion of monomer, τ_m is the rotational correlation time of the monomer, k is the ratio of the correlation time of the tetramer to that of the monomer, and τ_m^{obs} is the observed correlation time as determined from the measured relaxation rates. Based on CCL2 information, the rotational correlation time of the CCL27 tetramer structure was estimated using HYDRONMR as 20.2 ns. The corresponding monomeric correlation time was calculated to be 6.5 ns giving a value for k of 3.1. Using the observed isotropic correlation time of 9.2 ns this yielded a value x of 0.67, so that a mixture would be approximately two-thirds monomer and one-third tetramer, in order to result in an observed weighted average species with representative properties of the dimers. Reconsidering the results from the translational diffusion measurements, such a monomer-tetramer equilibrium would result in an observed D_s of 1.1×10^{-10} m^2/s, similar to the experimentally determined value.

All of the above methods reach a consistent picture that at 1.0 mM CCL27 the observed weighted average corresponds to a dimer species, while there are interactions between multiple interfaces that ultimately contribute to the tetramer structure, a behavior which contrasts with many chemokines that adopt discrete oligomerization states at a given concentration.

Supplemental References

1. Altieri, A. S. (1995) *Journal of the American Chemical Society* **7**, 740-743
2. Wishart, D. S., and Sykes, B. D. (1994) *J Biomol NMR* **4**(2), 171-180
3. Linge, J. P., O'Donoghue, S. I., and Nilges, M. (2001) *Methods Enzymol* **339**, 71-90
4. Nilges, M., and O'Donoghue, S. I. (1998) *Progress in Nuclear Magnetic Resonance Spectroscopy* **32**, 107-139
5. Brunger, A. T., Adams, P. D., Clore, G. M., DeLano, W. L., Gros, P., Grosse-Kunstleve, R. W., Jiang, J. S., Kuszewski, J., Nilges, M., Pannu, N. S., Read, R. J., Rice, L. M., Simonson, T., and Warren, G. L. (1998) *Acta Crystallogr D Biol Crystallogr* **54**(Pt 5), 905-921
6. Cornilescu, G., Delaglio, F., and Bax, A. (1999) *J Biomol NMR* **13**(3), 289-302
7. Hwang, T. L., Van Ziil, P. C. M., and Mori, S. (1998) *Journal of Biomolecular NMR* **11**(2), 221-226
8. Ghose, R., and Prestegard, J. H. (1998) *J Magn Reson* **134**(2), 308-314
9. Wang, C. (2003) *Journal of the American Chemical Society* **125**(30), 8968 - 8969
10. Millet, O. (2000) *Journal of the American Chemical Society* **122**(12), 2867 - 2877
11. Luz, Z. (1963) *the Journal of chemical physics* **39**(2), 367 - 370

Supplemental Figure Legends

SF. 1. Examples of chemokine oligomerization. A: Dimer structure for CCL2 showing a standard CC chemokine dimer with two small β-strands at the interface formed by the N-terminal regions of both subunits, monomeric subunits colored in yellow and red. B: Dimer structure for CXCL8, a CXC chemokine dimer with the interface predominantly formed between residues on the first β-strand of each subunit. Monomeric subunits are colored red and green. C: Tetramer structure for CCL2. The tetrameric form of CCL2 has characteristics of both a CC dimer as shown in A, and a CXC dimer shown in B. The

monomeric subunits are colored in cyan, yellow, red, and green, to emphasize CC and CXC interfaces. D: The same CCL2 tetramer as in C, viewed from the top in order to better visualize the CXC dimer interface.

SF. 2. Pulsed Field Gradient (PFG) diffusion analysis of CCL27 in order to evaluate the effects of different buffer conditions and pH on the oligomeric state.

SF. 3. A: R_1, values for 1.0 mM CCL27. B: Comparison of R_2^{CPMG} rates (blue) with $R_2^0 = \kappa\eta_{xy}$ (pink) for 1.0 mM CCL27 at 500 MHz. The majority of residues possess significant residual exchange contributions to their transverse relaxation rates measured using fast CPMG pulsing. C: $[^1H]^{15}N$ heteronuclear NOE values for 1.0 mM CCL27 at 500 MHz.

SF. 4. ^1H-^{15}N (HN)CH-NOE of CCL27 at 2.0 mM, 50/50 ^{15}N labeled (^{13}C-depleted), ^{13}C labeled sample of CCL27, prepared in 50 mM acetate, pH 5.6. Additional peaks relative to the 3.0 mM sample are indicated by boxes.

SF. 5. ^1H-^{15}N HSQC analysis of CCL27 as a function of concentration. A: Changes in chemical shift values between the 3.0 mM (where there is substantial tetramer) and 0.025 mM samples (where it is primarily monomeric). B: Changes in chemical shift values between the 1.0 mM (where it is primarily dimeric) and 0.025 mM. The red lines in both spectra indicated changes above baseline.

SF. 6. A: Exchange contributions for 1.0 mM CCL27 at 600 MHz from fitting the TROSY-selected spin-echo experiment. B: Two orthogonal views of the monomeric CCL27 structure showing the five exchange "hotspots" identified from the TROSY-selected spin-echo exchange experiment colored red.

SF. 7. PFG diffusion analysis of WT and mutant CCL27. A: Monomeric structure of CCL27, N-terminal truncation mutant residues shown as lines [3-88] CCL27 and [6-88] CCL27 (red), proline mutations (green), C-terminal truncation mutant [1-73] CCL27 (blue), truncated two residues to the C-terminal side of the α-helix. B: PFG diffusion results for mutations of the two N-Terminal proline residues to alanine (P4A, P5A). C: PFG diffusion analysis of the C-Terminal truncation mutant [1-73] CCL27.

SF. 8. Chemical cross linking of CCL27 in the absence of GAGs using Sulfo-EGS . Concentrations are indicated above the gel and the presence of Sulfo-EGS is indicated below.

Supplemental Table 1: Hydrodynamic radii

A

Conc. (mM)	D_t x 10^{-10} m^2/s	r_h (nm)	*M* (kDa)
0.05	1.26	1.88	13.4
0.1	1.26	1.89	13.7
0.2	1.25	1.89	13.8
0.5	1.19	1.98	15.8
1.0	1.09	2.15	20.1
1.75	1.03	2.25	23.2
2.1	0.96	2.41	28.5
3.5	0.84	2.68	39.1

B

Tetrameric Proteins	M (kDa)	r_h (nm)
CCL2	34.3	2.65
CX_3XL1	31.5	2.7
CXCL10-H	34.6	2.6
CXCL10-M	34.6	2.55
CXCL10-T (β-strands)	34.6	2.57
CCL14_1	34.8	2.75
CCL14_2	34.8	2.73
Dimeric Proteins		
MCP-1	17.4	2.51
CCL14		
CCL4 (Mip1B)	15.7	2.33
CXCL8 (CXCL8)	16.6	2.33
CXCL10-H (CXCL10)	17.3	2.20
CXCL10-T (CXCL10)	17.3	2.05
Monomeric Proteins (controls)		
CCL27	10.2	1.87
CCL2	8.7	1.84
CXCL8	8.3	1.82
CXCL10	8.7	1.83

Supplemental Table 1: A: Variation in the translational diffusion constant, hydrodynamic radius and estimated molecular weight with concentration of CCL27 over the range 0.05 mM to 3.5 mM, using HydroNMR. B: Calculated Hydrodynamic ratios (r_h) from atomic structures using Hydropro

Supplemental Table 2: Diffusion Tensor Results

Model	Parameter	500 MHz data	600 MHz data
Axially symmetric, oblate	D_{perp} / 10^7 s^{-1}	2.08 ± 0.04	2.06 ± 0.03
	D_{par} / 10^7 s^{-1}	1.44 ± 0.05	1.43 ± 0.04
	χ^2_{exp}	133	132
	χ^2_{sim}	55	57
Axially symmetric, prolate	D_{perp} / 10^7 s^{-1}	1.73 ± 0.02	1.74 ± 0.01
	D_{par} / 10^7 s^{-1}	1.99 ± 0.03	2.09 ± 0.05
	χ^2_{exp}	156	172
	χ^2_{sim}	55	56
Fully anisotropic	D_{xx} / 10^7 s^{-1}	2.11 ± 0.05	2.10 ± 0.04
	D_{yy} / 10^7 s^{-1}	2.00 ± 0.05	2.03 ± 0.04
	D_{zz} / 10^7 s^{-1}	1.47 ± 0.05	1.42 ± 0.05
	χ^2_{exp}	128	131
	χ^2_{sim}	53	55

Supplemental Table 2: Results from fitting the rotational diffusion tensor using TENSOR2. The principal components are listed for the two axially symmetric models (oblate and prolate) and the fully anisotropic models. χ^2_{exp} is the experimental χ^2 value and χ^2_{sim} the MC-derived 95 % confidence limit.

Supplemental Table 3: Magnitudes of diffusion tensors, CC and CXC

	CC-dimer (1)	CC-dimer (2)	CXC-dimer
D_{xx} / 10^7 s^{-1}	0.97	0.80	1.55
D_{yy} / 10^7 s^{-1}	0.98	0.82	1.65
D_{zz} / 10^7 s^{-1}	2.11	1.63	1.93

Supplemental Table 3: Magnitudes of the principal components of the anisotropic diffusion tensors for CC-type and CXC-type dimer models of CCL27, as determined using the program HYDRONMR. The first and second CC-type dimers were modelled from the monomeric structure with the flexible C-terminus removed (1) and intact (2).

Supplemental Figure 1

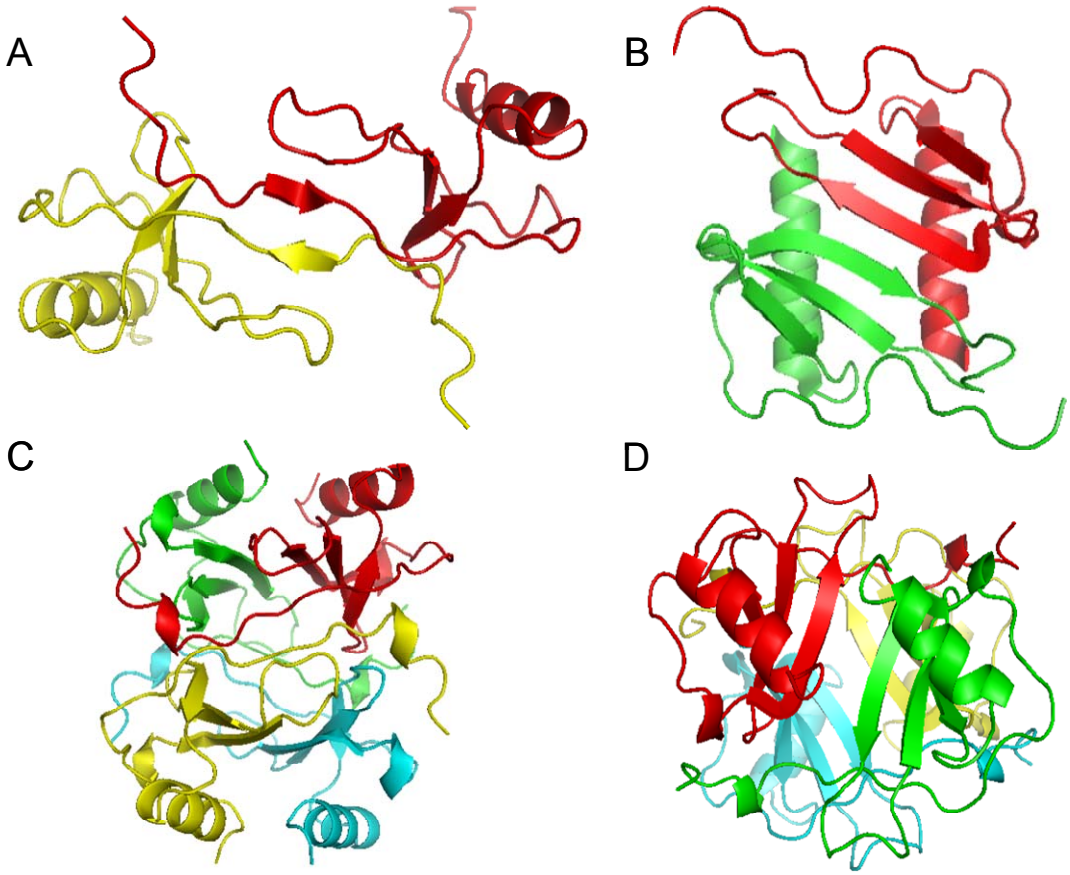

Supplemental Figure 2

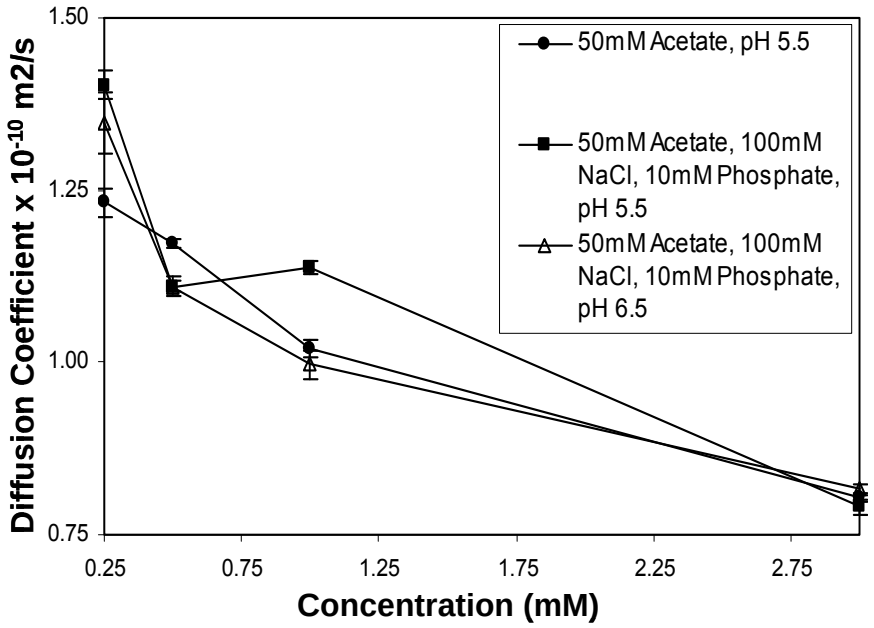

Supplemental Figure 3

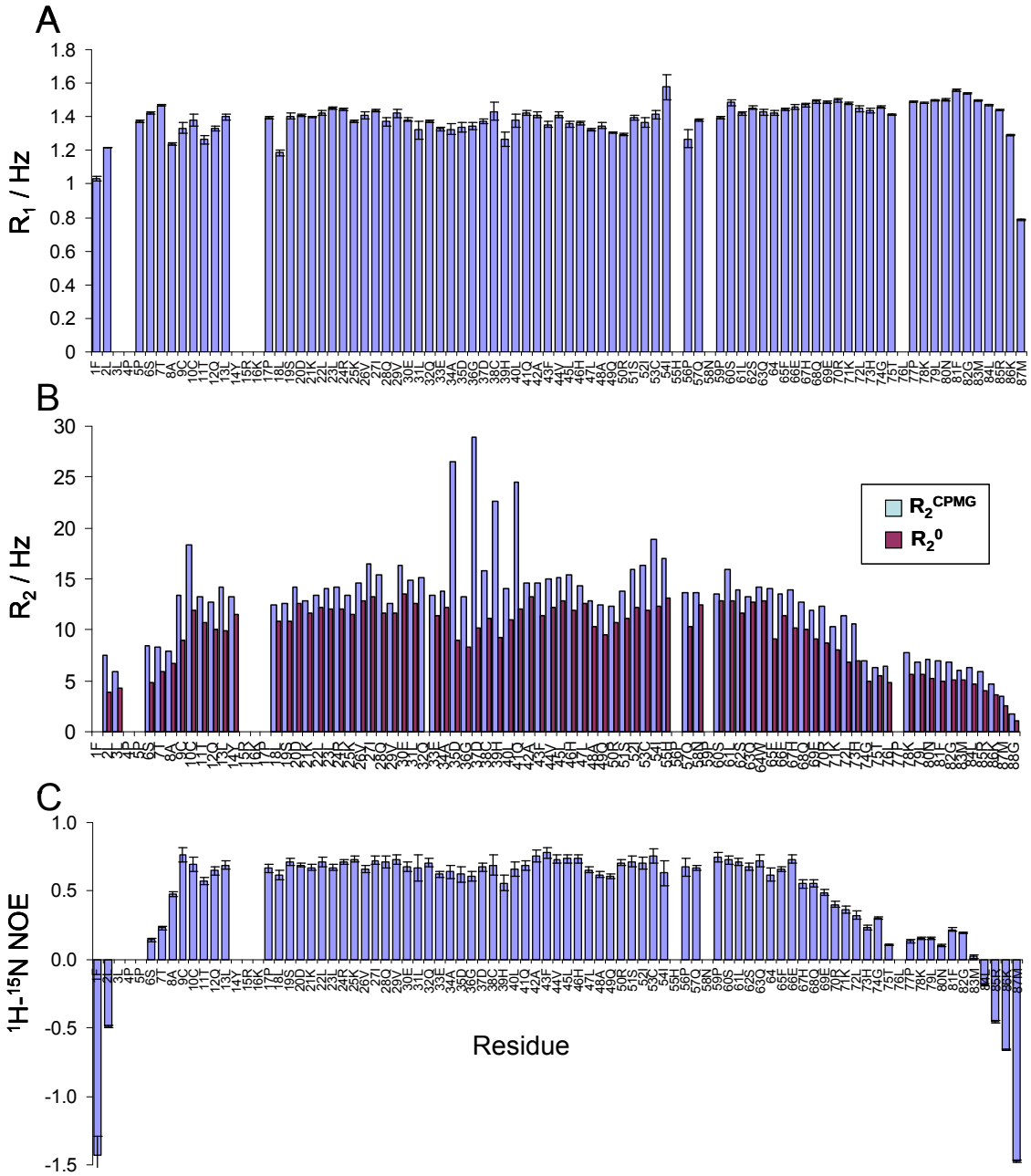

Supplemental Figure 4

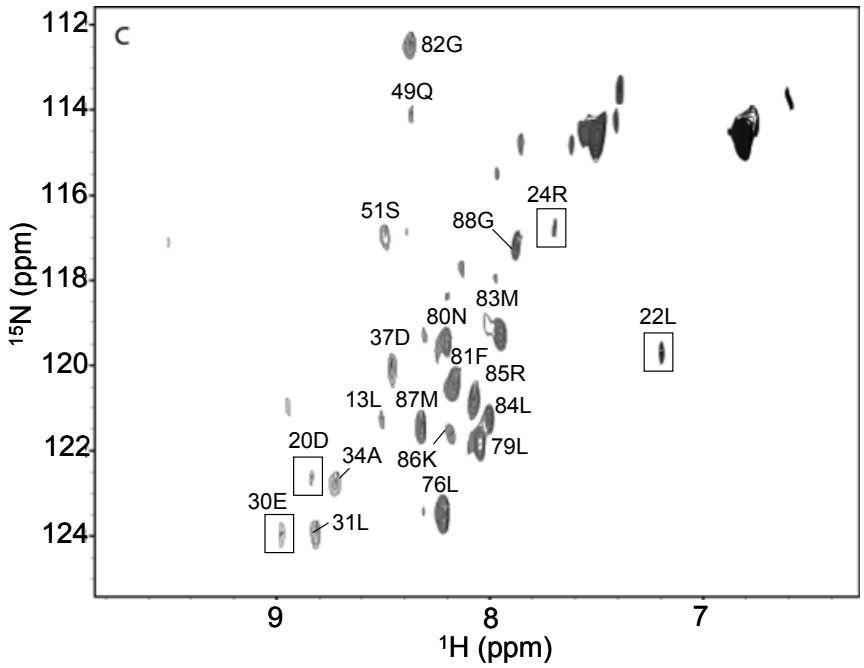

Supplemental Figure 5

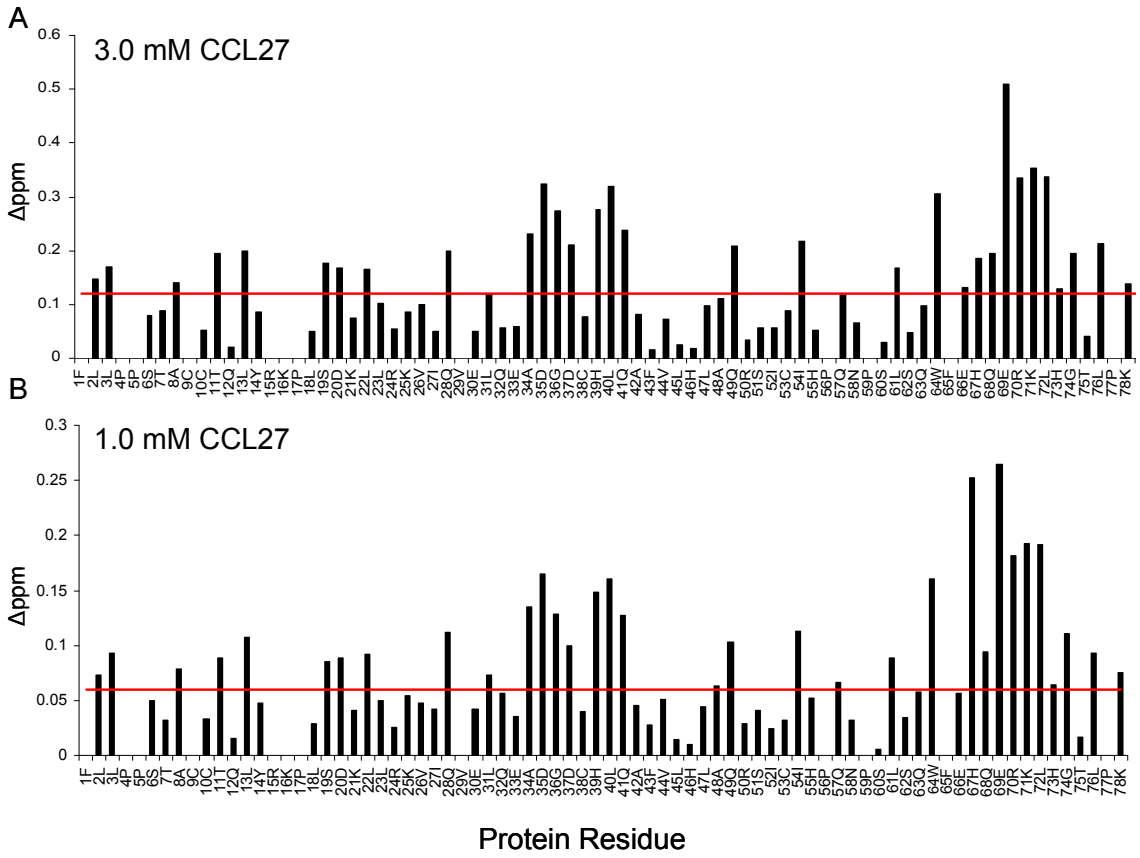

Supplemental Figure 6

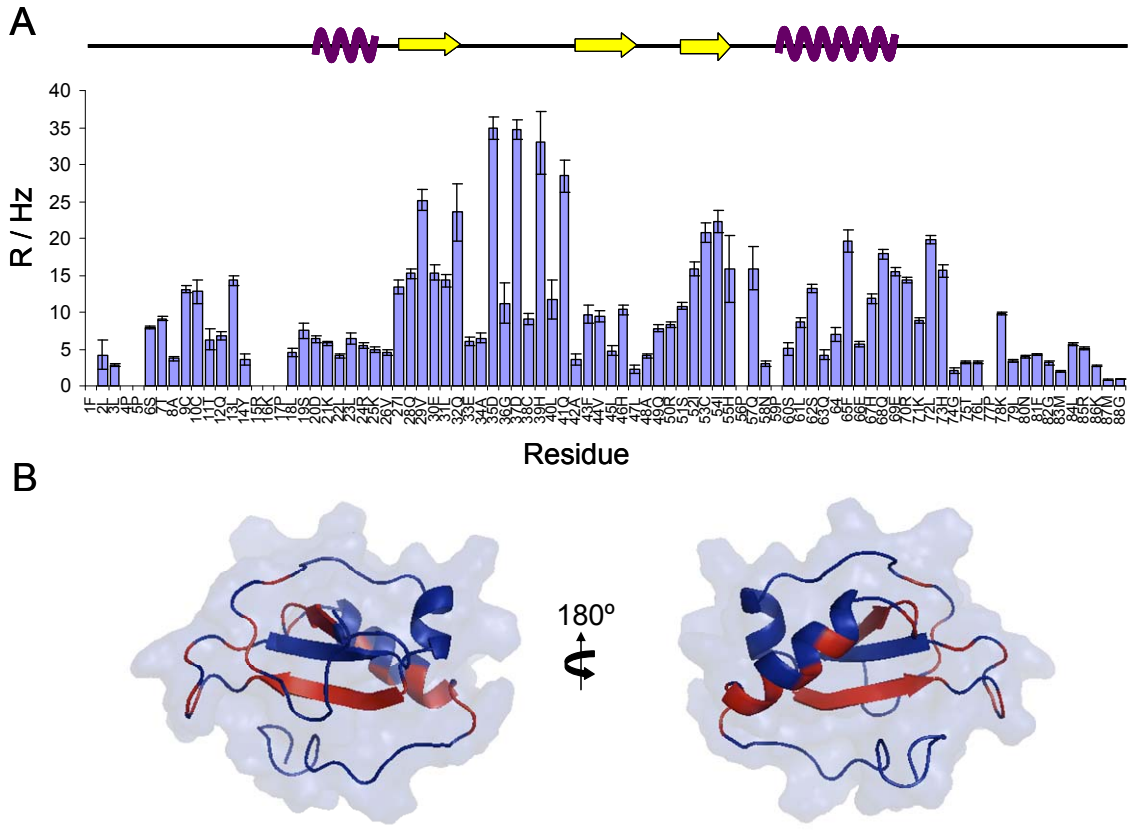

Supplemental Figure 7

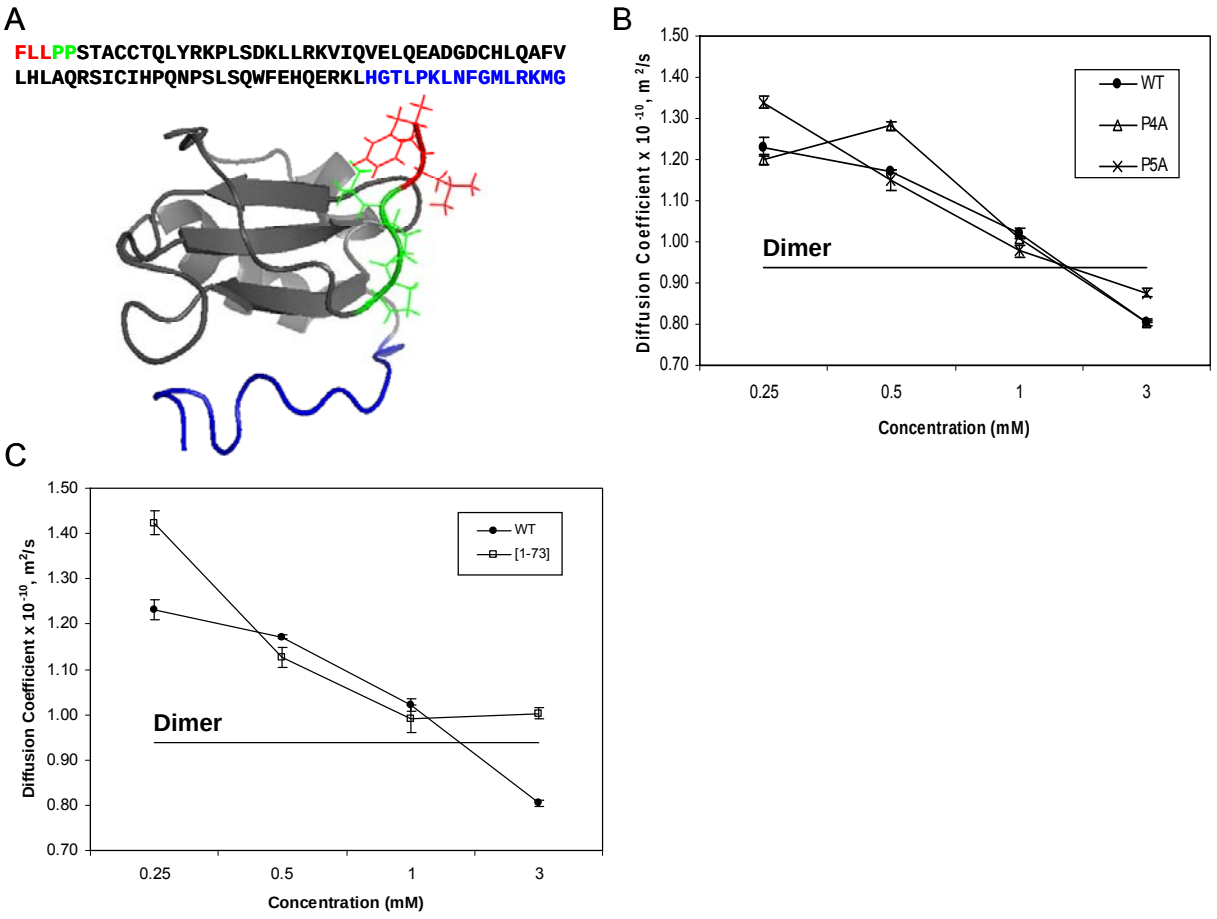

Supplemental Figure 8